Electronic materials

Achieving high thermoelectric properties of Bi_2S_3 via $InCl_3$ doping

Jun Guo[1] ⓘ, Zhen-Hua Ge[1,*] ⓘ, Feng Qian[1] ⓘ, De-Hong Lu[1] ⓘ, and Jing Feng[1] ⓘ

[1] Faculty of Materials Science and Engineering, Kunming University of Science and Technology, Kunming 650093, China

ABSTRACT

Bi_2S_3, with earth-abundant compositions and a low thermal conductivity, is regarded as a candidate thermoelectric material. In this work, Bi_2S_3 samples that were doped with x % mol $InCl_3$ were successfully fabricated via a mechanical alloying and spark plasma sintering process. $InCl_3$, as an n-type donor dopant, was added to the Bi_2S_3 system to improve its electrical transport properties and optimize its thermal conductivity. Upon doping, the electrical conductivity of Bi_2S_3 doped with 1 mol% $InCl_3$ reaches up to 62 Scm^{-1}, and the Seebeck coefficient maintains a relatively large value of -244 $\mu V\ K^{-1}$ at 673 K, which results in a maximum power factor of 363 $\mu W\ m^{-1}\ K^{-2}$. Furthermore, due to a simultaneously reduced thermal conductivity at high temperature, a ZT peak of 0.57 is obtained at 673 K along the parallel to the press direction for the sample doped with 1.0 mol% $InCl_3$, which is almost four times higher than that of pristine Bi_2S_3 (0.14 at 673 K). The elastic properties and Debye temperature of Bi_2S_3 are also calculated to analyze the origin of the intrinsically low thermal conductivity and are compared to those of other thermoelectric materials with a low thermal conductivity.

Introduction

Given the great increasing demand for clean renewable energy, thermoelectric materials are considered to be an effective method to alleviate the energy crisis [1]. Thermoelectric (TE) materials offer a recipe to provide a green, clean and renewable source of energy by converting waste heat directly into electrical energy [2, 3]. The conversion efficiency of TE materials can be estimated by the figure of merit (ZT), which is defined as $ZT = (\alpha^2\sigma/\kappa)T$, where σ is the electric conductivity, α is the Seebeck coefficient, κ is the thermal conductivity and T is the temperature in kelvin. Notably, a high power factor ($\alpha^2\sigma$) and a low value of κ are required for efficient TE materials. However, the laws of physics affect this situation of ours synchronously. The Wiedemann–Franz law indicates there is a strong coupling between σ and κ, and the Pisarenko relation reveals that α is inversely proportional to the concentration of carriers (n); therefore, it is difficult to optimize these parameters independently. To gain a relative high ZT value,

several methods were attempted, such as doping to improve the carrier concentration (n) and carrier mobility (μ) simultaneously [4, 5], nano-structuring engineering and compositing to reduce the lattice thermal conductivity (κ_L) [6–8], and band engineering to modify the Seebeck coefficient (S) and effective mass (m^*) [9, 10].

Aside from a high performance, low toxicity and cost also require crucial consideration. It is known that Bi_2Te_3-based [11] and PbTe-based [12] thermoelectric materials have been investigated for decades owing to the excellent TE properties during a certain temperature range. Because Pb is toxic and Te is lacking in earth's crust, the rich abundance and environmental benignity of sulfur-based composites have attracted attention as promising alternative TEs [13–17]. Bismuth sulfide (Bi_2S_3), which has intrinsically low thermal conductivity, has been investigated as an underlying TE material for a long time owing to its potential TE properties. However, similar to most TE materials of low thermal conductivity, such as SnSe [18–20], BiCuSeO [5, 21, 22] and Bi_2O_2Se [23, 24], high electrical resistivity restricts their widespread application. It has been widely demonstrated that more electrons will be generated when halogen group elements (Cl, Br and I) are doped at the S site [13, 25, 26]. Furthermore, plenty of thermoelectric materials obtain a giant leap in performance due to the introduction of elemental indium (In) [27–29]. Herein, indium chloride ($InCl_3$) is used as an n-type dopant to optimize the electrical transport properties of Bi_2S_3.

Mechanical alloying (MA) has been utilized to prepare nanoscale materials due to its unique advantages, such as the production of uniform compositions and short fabrication times. Additionally, spark plasma sintering (SPS) is a suitable hot-sintering process for preparing nanoscale bulk materials due to its heating and cooling processes being achieved in a very short time, making it possible to inhibit the excessive growth of grains during the heat preservation process. In this work, the effect of $InCl_3$ doping on the electrical transport and thermal transport properties of Bi_2S_3 has been investigated. The elastic properties of Bi_2S_3 have been also calculated to compare with low thermal conductivity materials to further analyze the origin of low thermal conductivity. The results reveal that the combination of low thermal conductivity and an effectively enhanced power factor, a ZT peak of 0.57, is obtained for Bi_2S_3 doped with 1.0% mol $InCl_3$ at 673 K.

Experimental section

Synthesis

The Bi_2S_3 powders nominally doped with x mol% $InCl_3$ (x = 0, 0.25, 0.5, 1.0 and 1.5) were prepared by adding the appropriate proportion of high-purity Bi (99.9%), S (99.9%) and $InCl_3$ (99.99%) starting materials to mechanical alloy in a planetary ball mill (QM-3SP2, Nanjing University, China) at 425 r for 12 h. Then, a stainless steel vessel and balls were used, and the ratio of ball to powder weight was maintained at 20:1, as before [30]. The as-prepared Bi_2S_3 samples were densified in a Φ15-mm graphite mold under an axial pressure of 40 MPa using a spark plasma sintering (SPS) system (Sumitomo SPS632 lx, Japan) under vacuum at 673 K for 5 min. The detailed sintering process is shown below: Firstly, the pressure rose to 40 MPa during 1 min; next, the temperature was increased from room temperature to 623 K in 4 min, then increased to 673 K in 1 min and held at this temperature for 5 min and subsequently decreased to room temperature.

Characterization

X-ray diffraction (XRD) patterns were recorded on a MiniFlex 600 using Cu Kα1 radiation (40 kV, 15 mA, λ = 1.541 Å, step size = 0.02°, 5°min^{-1} from 20° to 70°). Field emission scanning electron microscopy (FE-SEM, Zeiss; Sigma 300, Germany) was used to characterize the fractured surface morphologies of all samples. The electronic absorption spectra of pristine and doped Bi_2S_3 samples were characterized on a Shimadzu UV-3600 plus UV–Vis–NIR spectrophotometer using an integrating sphere accessory. The transverse and longitudinal acoustic velocities were measured using an UMS Advanced Ultrasonic Modulus measurement system (Techlab, France). The bulk sample was cut and polished into disk shape of Φ6 mm × 1 mm for the measurement of the sound speed. Then, the transverse phonon velocity and the longitudinal phonon velocity were measured via transverse probe (V157-RM, 5 MHz) and longitudinal probe (V116-RM, 20 MHz) under the voltage of 50 V and 250 V, respectively.

Thermoelectric performance characterization

The obtained bulk samples were cut and ground into disk shapes of Φ6 mm × 1.5 mm and bars of 2 mm × 2 mm × 10 mm for the measurements of the thermal diffusivity coefficient and electrical properties, respectively. The measurements of the thermal and electrical transport behavior in this work were done along the parallel to the press direction of the SPS. The electrical resistivity and Seebeck coefficient of the bulk samples were measured using a Seebeck coefficient/electrical resistance measuring system (ZEM-3, Ulvac-Riko, Japan) from 323 to 673 K under the protection of a helium atmosphere. The thermal conductivity (κ) was calculated by the correlation $\kappa = DCp\rho$, where the thermal diffusivity coefficient (D) was measured by the laser flash method (LFA457, Netzsch, Germany), the specific heat (Cp) was measured by thermal analysis (STA449, Netzsch, Germany), and the sample density (ρ) was determined according to the Archimedes method, i.e., $\rho = \frac{M_O}{M_2 - M_1}\rho_h$, where M_O is the quality of the dry sample in air, M_2 is the quality of the sample in air after fully absorbing water, M_1 is the quality of the sample in water after fully absorbing water and ρ_h is the density of water. Additionally, the porosity was obtained via subtracting the relative density of the actual sample from the relative density of the fully dense bulk sample, namely $P = \rho_0/\rho_0 - \rho/\rho_0 = 1 - \rho/\rho_0$, where ρ is the actual density, ρ_0 is the theoretical density.

Results and discussion

Figure 1a reveals typical powder X-ray diffraction (XRD) patterns of the $Bi_2S_3 + x$ mol% $InCl_3$ ($x = 0$, 0.25, 0.5, 1.0, 1.5) samples. All main peaks are well matched with orthorhombic Bi_2S_3 (PDF#75-1306) in the *Pbnm* space group. After the spark plasma sintering (SPS) process, all diffraction peaks become narrower and sharp, indicating the random growth of grains (see Fig. 1b). Furthermore, a second phase appears as $x > 1.0$ and can be indexed as In_6S_7 (PDF#72-0011). As shown in Fig. 1c, the 2-theta angle of 28.5° for the pristine Bi_2S_3 bulk sample is slightly lower than the 28.6° that is given by the standard card, and this difference is due to the volatilization of S during the SPS process. The enlarged patterns of

the 2-theta range from 28° to 29° for Bi_2S_3 samples reveal a shift after $InCl_3$ doping. The main peak for the (2 3 0) plane moves to higher angles when $x < 1.0$ and then shifts back, which implies a lattice deformation of Bi_2S_3. Considering that the ionic radius of Cl (0.181 nm) is quite close to that of S (0.184 nm), the rightward shift in the diffraction peaks is attributed more to the substitution of In (0.08 nm) at the Bi (0.103 nm) site. When $x \geq 1.0$, the expansion of the host lattice is likely due to a portion of In^{3+} entering the interstitials of the Bi_2S_3 lattice to increase the lattice parameter. The lattice parameter variations of all $InCl_3$-doped Bi_2S_3 samples are obtained by refining the bulk sample XRD data. The lattice parameters are found to change along all three axes. The volume of the unit cell first decreases and then increases with the $InCl_3$ doping content, as plotted in Fig. 1d, which is a good match with the shift direction of XRD and with the details we discussed above.

Figure 1e shows the electronic absorption spectra of pristine and doped Bi_2S_3 powders, and the insert presents the obtained band gap values. It is widely known that Bi_2S_3 is a direct band gap semiconductor, and the optical band gap can be estimated according to the Kubelka–Munk theory [31, 32]: $F(R)*(hv) = (hv - E_g)^{1/2}$, where R, F(R), h, v and E_g are the reflectance, the proportional to the extinction coefficient, Planck's constant, the frequency of light and the band gap, respectively. After a series of transformations, the pristine Bi_2S_3 has a band gap value of 1.328 eV, which is quite close to the theoretical value reported before [33]. Upon $InCl_3$ doping, the electronic absorption spectra of $Bi_2S_3 + x$ mol% $InCl_3$ reveal an initial shift in the absorption edge to a lower energy when $x = 0.25$ and then moves to higher energies as $x > 0.25$. The band gap values of all samples are 1.328 eV, 1.309 eV, 1.317 eV, 1.324 eV and 1.332 eV. From the shift in the XRD diffraction and the variation trend of the lattice parameters and band gap values as a function of $InCl_3$ doping content, it is not hard to conclude that the $InCl_3$ is successfully introduced into the Bi_2S_3 lattice.

The fractographic results for pristine Bi_2S_3 and all Bi_2S_3 bulk samples doped with x mol% ($x = 0.25$, 0.5, 1.0 and 1.5) $InCl_3$ fractured in the direction parallel to the SPS press direction are presented in Fig. 2. The orthorhombic layered structure of pristine Bi_2S_3 with an average grain size of 400 nm is shown in Fig. 2a. The grain size decreases with increasing x up to 0.5 and then increases when x is greater than 1.0, which
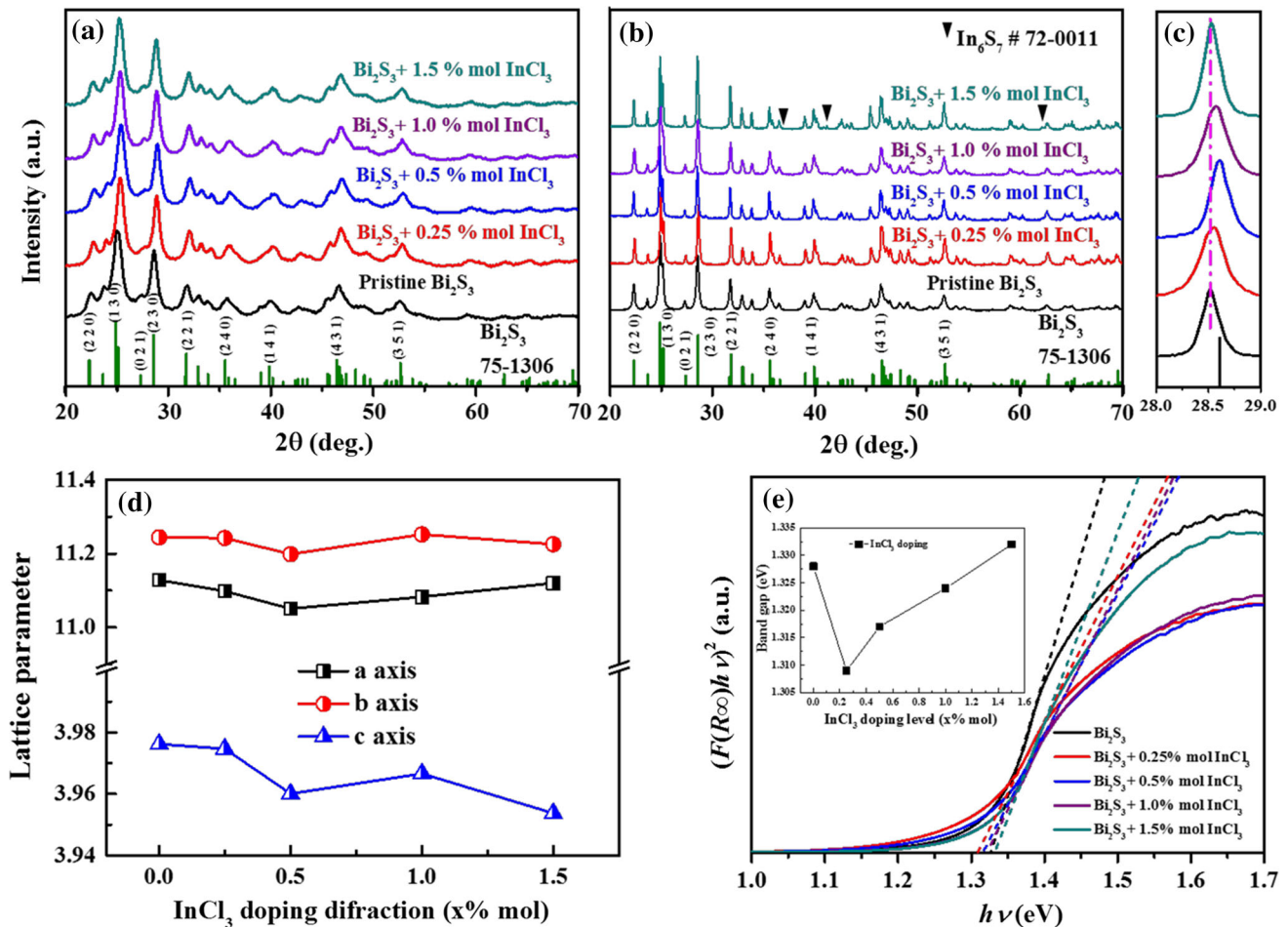
Figure 1 XRD patterns of $Bi_2S_3 + x$ mol% $InCl_3$ (x = 0, 0.25, 0.5, 1.0, 1.5) **a** powders, **b** SPSed bulks and **c** enlarged patterns in 2-theta range of 28°–29°; **d** lattice parameter of $Bi_2S_3 + x$ mol% $InCl_3$; **e** electronic absorption spectra. Insert shows the band gap variation.

is perhaps ascribed to the activation of lattice deformation by introducing $InCl_3$ [34]. Upon $InCl_3$ doping, the grain size variation in the Bi_2S_3 system agrees well with the changes in lattice parameters. Additionally, compared to those of the pristine Bi_2S_3 bulk sample, the number of pores increases after doping, which leads to low density and relative density. The densities of pristine Bi_2S_3 and Bi_2S_3 doped with x mol% $InCl_3$ (x = 0.25, 0.5, 1.0 and 1.5) are 6.579, 6.372, 6.389, 6.242 and 6.418, respectively, and the relative densities of all samples are greater than 90%, as shown in Fig. 2f. The increased pores also play a significant role in reducing the lattice thermal conductivity, and the details will be discussed later.

The electrical transport properties as a function of the measured temperature for all samples ($Bi_2S_3 + x$ % mol $InCl_3$, x = 0, 0.25, 0.5, 1.0 and 1.5) are shown in Fig. 3. The electrical conductivities of pristine and $InCl_3$-doped Bi_2S_3 samples increase with

temperature, which indicates characteristic semiconductor behavior. Additionally, even the electrical conductivity value for pristine Bi_2S_3 increases from 0.14 Scm^{-1} at 323 K to 5 Scm^{-1} at 673 K, which remains a long way from that of high-performance thermoelectric materials. The extremely low electrical conductivity originates from the intrinsically low carrier concentration. With the addition of $InCl_3$, the electrical conductivities of all samples show an upward tendency over the measured temperature range. The maximum value of 62 Scm^{-1} is obtained for the $Bi_2S_3 + 1.0$ mol% $InCl_3$ bulk sample at 673 K. Then, the electrical conductivity begins to decrease as the dopant content rises above 1.0 mol%, which is ascribed to carrier scattering caused by defects induced via doping. After $InCl_3$ is added to the host matrix, there are two kinds of defect reactions corresponding to substitutional and interstitial equations, which are expressed as follows:
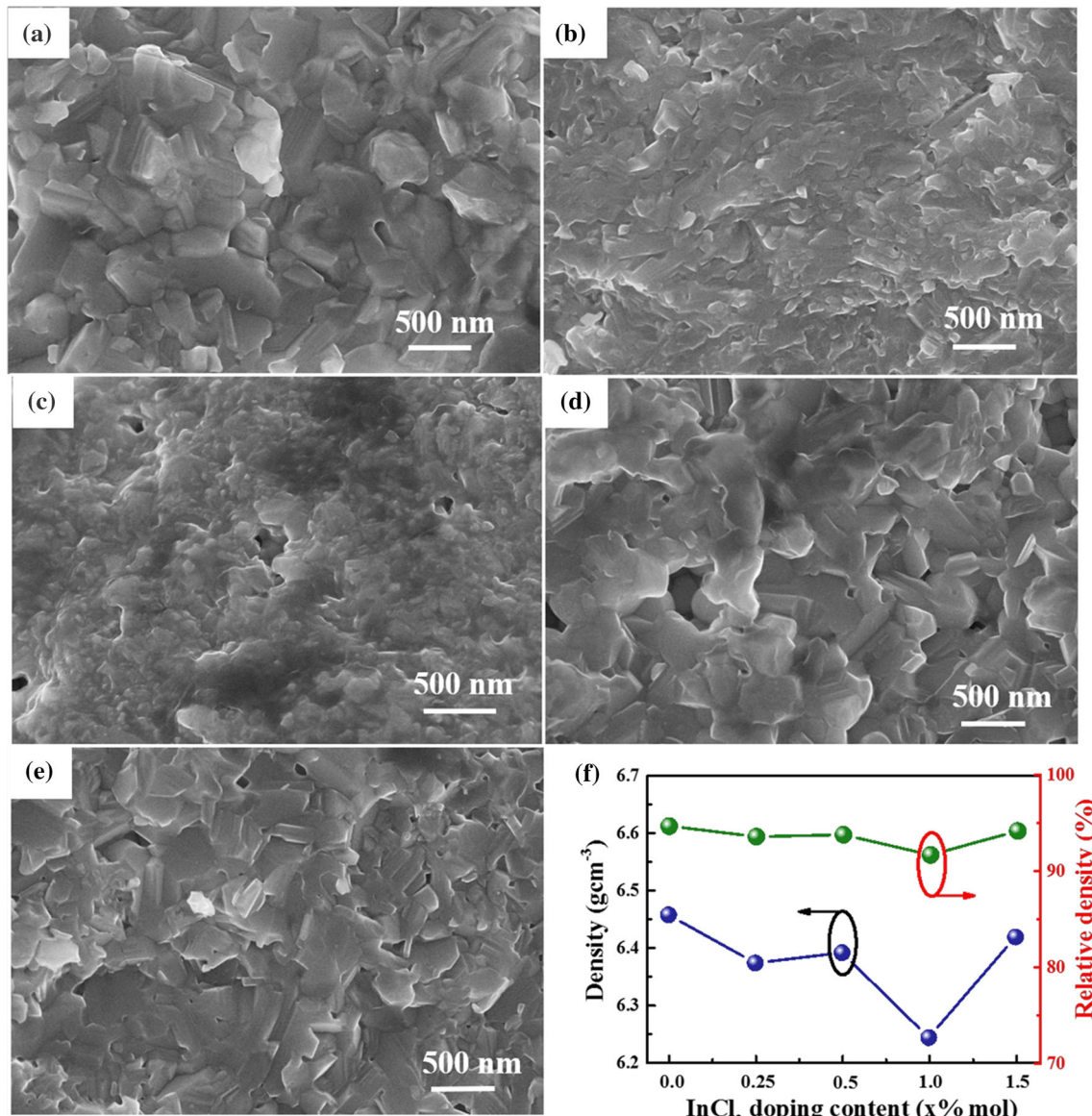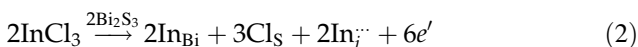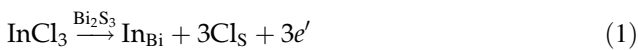
Figure 2 FE-SEM image (**a–e**) of the fractured surfaces along the parallel to the press direction and density and relative density (**f**) of Bi$_2$S$_3$ + x mol% InCl$_3$ bulks. **a** x = 0, **b** x = 0.25, **c** x = 0.5, **d** x = 1.0, **e** x = 1.5.

$$InCl_3 \xrightarrow{Bi_2S_3} In_{Bi} + 3Cl_S + 3e' \quad (1)$$

$$2InCl_3 \xrightarrow{2Bi_2S_3} 2In_{Bi} + 3Cl_S + 2In_i^{\cdot\cdot} + 6e' \quad (2)$$

When x < 1.0, InCl$_3$ substitutes the position of Bi$_2$S$_3$ to form a substitutional solid solution, resulting in the decrease in the lattice parameters. With x ≥ 1.0, a portion of the substitute InCl$_3$ enters the interstitial sites to form an interstitial solid solution, which leads to the increase in parameter. The increased lattice parameter is derived from the expansion of the unit cell volume. The electron concentration is increased when Cl$^-$ substitutes S^{2-} and further increased after In^{3+} enters the host lattice, as revealed in Eqs. (1) and (2). Owing to the high electrical conductivity appearing at high temperature, here, we assume that the electrical transport benefits from thermal activation and the carrier concentration, mobility and electrical conductivity are indicated as [8, 35, 36]

$$n(T) = AT^3e^{-B/T} \quad (3)$$

$$\mu(T) = CT^{-3/2} \quad (4)$$

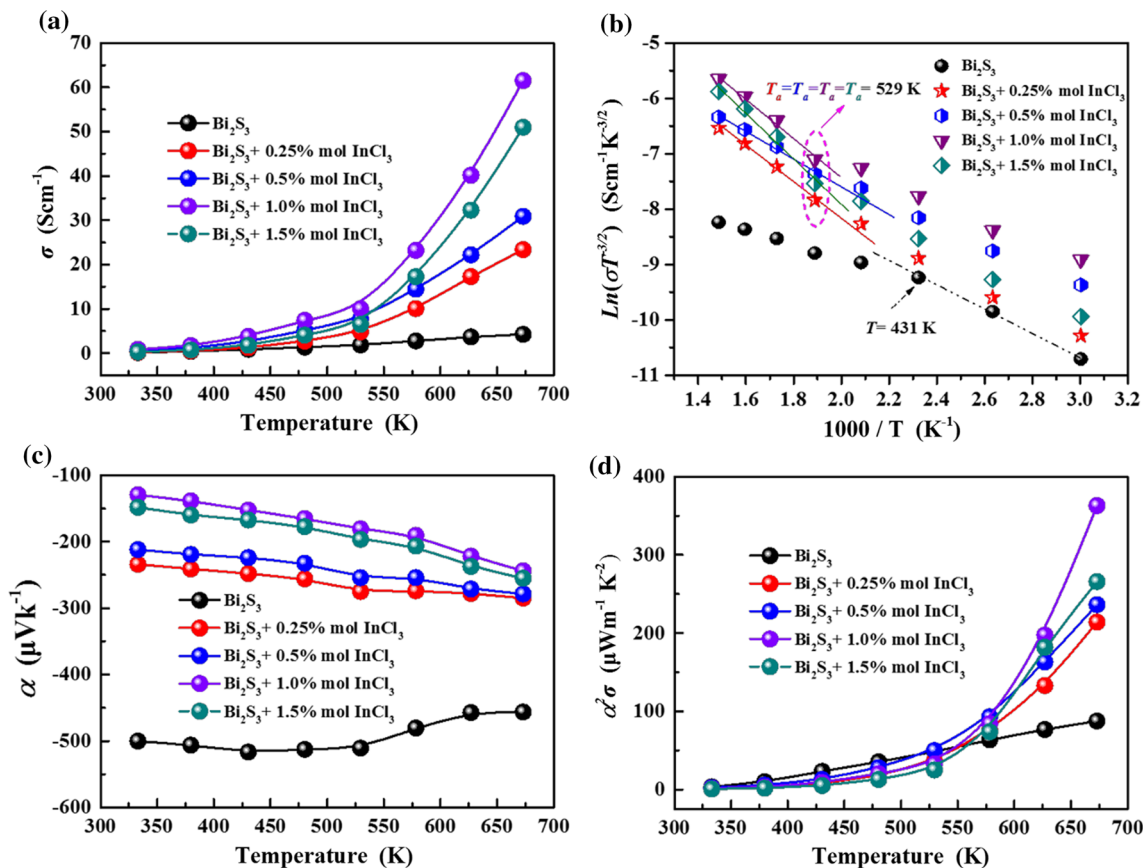$$\sigma = DT^{3/2}e^{-B/T} \quad (5)$$

Figure 3 Temperature-dependent electrical transport properties for all $Bi_2S_3 + x$ mol% $InCl_3$ samples ($x = 0$, 0.25, 0.5, 1.0, 1.5):
a electrical conductivity (σ), **b** thermal activation temperature, **c** Seebeck coefficient (S), **d** power factor (PF).

where A, B and C are parameters related to the material and D is a specific constant. An approximately linear relationship between $\ln(\sigma T^{-2/3})$ and $1000T^{-1}$ exists for all samples at high temperature. Here, the results in Fig. 3b indicate that thermal activation has a commanding influence on the electrical conductivity with increasing temperature. The thermal activation temperature (T_a) for all $InCl_3$-doped samples appears at 529 K, which is in good agreement with the temperature marking the rising point of electrical conductivity. Different from the doped samples, the undoped sample shows a weak thermal activation effect above 413 K.

Figure 3c shows the Seebeck coefficient dependence on the measured temperature for pristine and $InCl_3$-doped Bi_2S_3 samples. A negative Seebeck coefficient indicates an n-type electrical transport behavior with electrons contributing more to the whole transport process. The absolute value of the Seebeck coefficient of pristine Bi_2S_3 increases for a temperature range of 323–423 K and then gently

decreases above 423 K. The maximum Seebeck coefficient value of -517 μV K^{-1} is obtained at 423 K. With increasing $InCl_3$ doping content, the absolute value of the Seebeck coefficient of Bi_2S_3 decreases remarkably from -500 μV K^{-1} for pristine Bi_2S_3 to -130 μV K^{-1} for Bi_2S_3 doped with 1.0 mol% $InCl_3$ at 323 K, which is strongly correlated with the increase in carrier concentration. Upon $InCl_3$ doping, the absolute Seebeck coefficient of Bi_2S_3 increases monotonically with the temperature in the measured range. According to the Mott expression [37], $S = (\pi^2 k_B^2 T/3e)\{dn(E)/ndE + d\mu(E)/\mu dE)_{E=E_F}$, the carrier concentration simultaneously affects the absolute value of the Seebeck coefficient along with the carrier mobility. Therefore, when the dopant content surpasses 1.0% mol, the increase in the Seebeck coefficient is probably due to a reduced carrier mobility, suggesting that the electron mobility influences the Seebeck coefficient to a greater extent than carrier concentration.

The power factor is significantly enhanced upon InCl$_3$ doping, particularly for 1.0% mol InCl$_3$ doping, which is improved by approximately five times than that of pristine Bi$_2$S$_3$. The maximum value of the power factor is obtained at 673 K as approximately 363 μW m^{-1} K^{-2} for Bi$_2$S$_3$ doped with 1.0 mol% InCl$_3$ and is benefited by the remarkably improved electrical conductivity and the relatively large Seebeck coefficient. The power factors of the Bi$_2$S$_3$ samples show an upward tendency similar to that of the electrical conductivity upon InCl$_3$ doping, which indicates that the electrical conductivity contributes more to the power factor when the Seebeck coefficient is large.

Figure 4 shows the thermal transport properties as a function of temperature for the pristine Bi$_2$S$_3$- and InCl$_3$-doped samples. The pristine Bi$_2$S$_3$ exhibits a relatively low total thermal conductivity (κ_{tot}), which may be ascribed to the interatomic bonding strength (the weak ionic and van der Waals forces) and to the lattice vibration anharmonicity. As revealed in Fig. 4a, κ_{tot} increases with the InCl$_3$ doping content, and κ_{tot} presents similar values when $x \geq 0.5$. Additionally, Bi$_2$S$_3$ doped with 1.5 mol% InCl$_3$ possesses the maximum κ_{tot}, with values ranging from 0.61 W m^{-1} K^{-1} at 323 K to 0.42 W m^{-1} K^{-1} at 673 K. The total thermal conductivity consists of two typical parts, the electrical thermal conductivity (κ_e) and the lattice thermal conductivity (κ_L), as follows: $\kappa_{tot} = \kappa_e + \kappa_L$. The value of κ_e can be obtained by $\kappa_e = L\sigma T$, where L, σ and T are the Lorenz number ($L = 2.45 \times 10^{-8}$ V^2 K^{-2}), electrical conductivity and temperature in kelvin, respectively. The value of κ_e is directly proportional to the electrical conductivity and herein exhibits an upward tendency similar to that of the electrical conductivity. The maximum κ_e of 0.1 W m^{-1} K^{-1} is achieved by the Bi$_2$S$_3$ sample doped with 1.0 mol% at 673 K (Fig. 4b). After subtracting κ_e, κ_L shows a relatively large value at low temperature and decreases with increasing temperature until a low κ_L of 0.32 W m^{-1} K^{-1} is finally obtained at 673 K for $x = 1.0$. A low κ_L has been
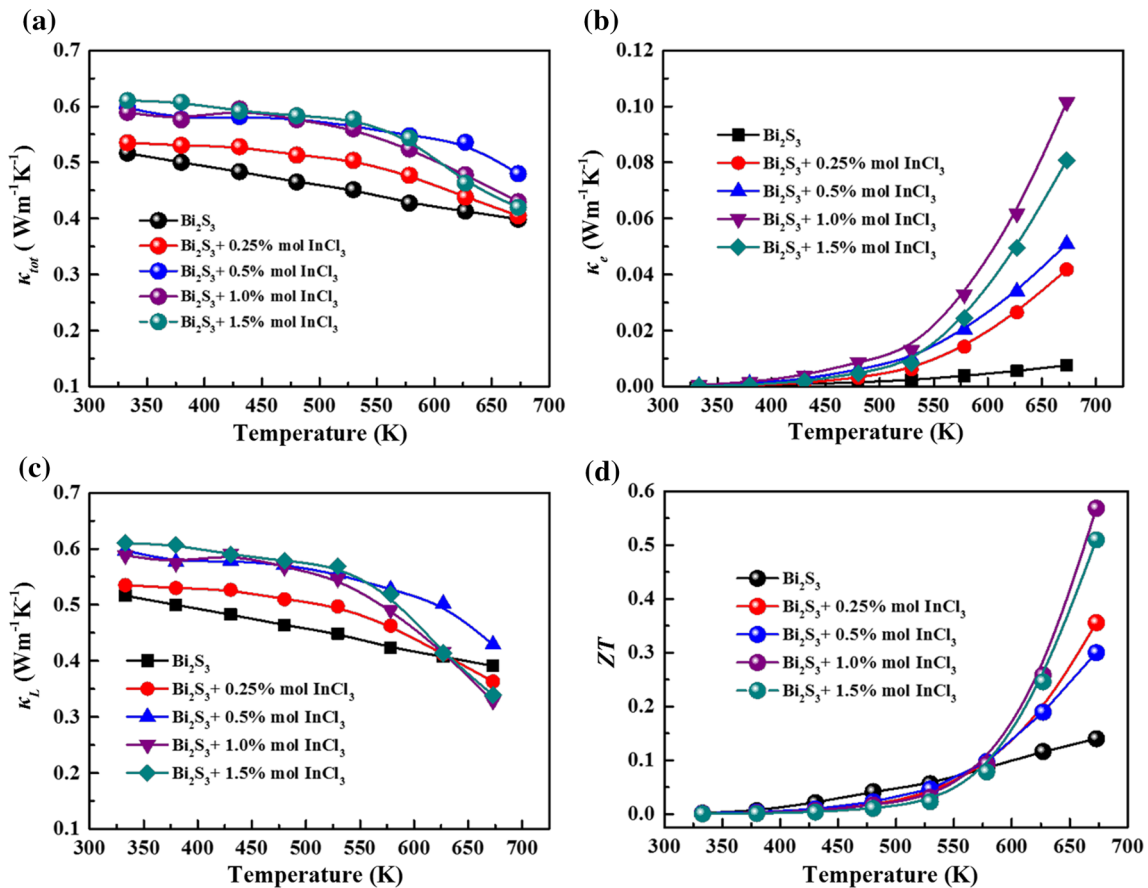

Figure 4 Temperature-dependent thermal transport properties for all Bi$_2$S$_3$ + x mol% InCl$_3$ samples (x = 0, 0.25, 0.5, 1.0, 1.5): **a** the total thermal conductivity (κ_{tot}), **b** electronic thermal conductivity (κ_e), **c** lattice thermal conductivity (κ_L), **d** ZT value.

proved to derive from the interatomic bonding type (ionic bond and covalent bond) and the lattice vibrations, apart from the abundance of pores in the host matrix. The effect of pores on reducing the lattice thermal conductivity is evaluated by the following formula [38]:

$$\kappa_L = \kappa_{L,f}\left(1 - \frac{4}{3}P\right) \tag{6}$$

where $\kappa_{L,f}$ is the lattice thermal conductivity of the full dense bulk material and P is the porosity, as listed in Table 1 ($P = 1 - \rho/\rho_0$, ρ/ρ_0 is the relative density). The $\kappa_{L,f}$ for the $Bi_2S_3 + x$ mol% $InCl_3$ samples ($x = 0, 0.25, 0.5, 1.0$ and 1.5) at room temperature are 0.541, 0.585, 0.651, 0.663 and 0.661 W m^{-1} K^{-1}, which suggests that the pores play an important role in scattering phonons to further reduce the lattice thermal conductivity. The rapidly dropped lattice thermal conductivity for Bi_2S_3 doped with 1.0, 1.5 mol% $InCl_3$ may be stem from the increased porosity and the generated secondary phase.

Furthermore, the ultrasonic pulse reflection method is used to evaluate the elastic properties and determine the origin of the low lattice thermal conductivity. On the basis of formulas (7) and (8) [39–41], a small Young's modulus (E) and Debye temperature (θ_D) and a large Grüneisen constant (γ) are necessary for a low lattice thermal conductivity.

$$\kappa_L \propto \frac{\rho^{1/6}E^{1/2}}{(M/n)^{2/3}} \tag{7}$$

$$\kappa_L = \frac{3.0 \times 10^{-5}M_a a \theta_D^3}{T\gamma^2 \upsilon^{2/3}} \tag{8}$$

$$E = \frac{\rho \upsilon_t^2(3\upsilon_l^2 - 4\upsilon_t^2)}{(\upsilon_l^2 - \upsilon_t^2)} \tag{9}$$

$$\upsilon_a = \left[\frac{1}{3}\left(\frac{1}{\upsilon_l^3} + \frac{2}{\upsilon_t^3}\right)\right]^{-1/3} \tag{10}$$

$$\upsilon_p = \frac{1 - 2(\upsilon_t/\upsilon_l)^2}{2 - 2(\upsilon_t/\upsilon_l)^2} \tag{11}$$

$$G = \frac{E}{2(1 + \upsilon_p)} \tag{12}$$

$$\gamma = \frac{3}{2}\left(\frac{1 + \upsilon_p}{2 - 3\upsilon_p}\right) \tag{13}$$

$$\theta_D = \frac{h}{k_B}\left[\frac{3N}{4\pi V}\right]^{1/3}\upsilon_a \tag{14}$$

where ρ, M, n, M_a, a^3, υ, υ_t, υ_l, υ_a, h, k_B, N, V, υ_p and G are the sample density, the atomic weight of the molecule, the atomic number of the molecule, the mean atomic weight of the constituent atoms, the average volume occupied by one atom, the lattice numbers of the primitive unit cell, the transverse phonon velocity, the longitudinal phonon velocity, the average phonon velocity, Planck's constant, the Boltzmann constant, the number of atoms in a unit cell, the unit cell volume, the Poisson ratio and the shear modulus, respectively. Here, the transverse phonon velocity (υ_t) and the longitudinal phonon velocity (υ_l) can be obtained via the ultrasonic pulse reflection method, while υ_a, υ_p, G, E, θ_D and γ can be calculated using Eqs. (10), (11), (12), (13) and (14) [39, 41–43]. The results are listed in Table 2.

The elastic properties of some typical materials with low lattice thermal conductivities are listed in Table 2 for comparison with those of Bi_2S_3. In this work, the average phonon velocity of Bi_2S_3 (1781 ms^{-1}) is lower than that of BiCuSeO (2107 ms^{-1}) and Bi_2Se_3 (2083 ms^{-1}), which results in the small Young's modulus of Bi_2S_3. It is worth noting that the covalent nature of a material decreases with the E value. Therefore, a small Young's modulus will weaken the covalent nature of a material to reduce the lattice thermal conductivity. Furthermore, the E of Bi_2S_3 is significantly lower than that of BiCuSeO (76.5 GPa) and Bi_2Se_3 (70.3 GPa) and is comparable to materials with ultralow lattice thermal conductivity, such as $BiSbSe_3$ (34.9 GPa) and $K_2Bi_8Se_{13}$ (37.1 GPa). Additionally, the Poisson ratio (υ_p) reflects the interatomic bonding type in a material; a small υ_p (0.1) value reveals a covalent bonding nature, whereas a typical υ_p value of 0.25 is obtained for

Table 1 Porosity (P), lattice thermal conductivity (κ_L) and lattice thermal conductivity of full dense ($\kappa_{L,f}$) of $Bi_2S_3 + x$ mol% $InCl_3$ bulk samples at room temperature

$Bi_2S_3 + x$ %mol $InCl_3$	$x = 0$	$x = 0.25$	$x = 0.5$	$x = 1.0$	$x = 1.5$
Porosity (%)	3.4	6.4	6.2	8.4	5.8
κ_L (Wm^{-1}K^{-1})	0.517	0.535	0.597	0.589	0.610
$\kappa_{L,f}$ (Wm^{-1}K^{-1})	0.541	0.585	0.651	0.663	0.661

Table 2 Comparisons of elastic properties of Bi_2S_3 and other materials with low thermal conductivity at room temperature

Parameter	Sample					
	Bi_2S_3	$BiSbSe_3$ [40]	BiCuSeO [22]	SnSe [41]	Bi_2Se_3 [45]	$K_2Bi_8Se_{13}$ [46]
v_l (ms^{-1})	2864	2815	3290	2730	3390	2683
v_t (ms^{-1})	1600	1455	1900	1250	1870	1438
v_a (ms^{-1})	1781	1629	2107	1420	2083	1605
E (GPa)	41.5	34.9	76.5	27.7	70.3	37.1
v_P	0.27	0.32	0.25	0.44	0.28	0.30
G (GPa)	16.3	13.2	30.6	9.6	27.5	14.3
γ	1.62	1.89	1.50	3.13	1.65	1.77
θ_D (K)	182	165	243	142	205	154

ionic materials [44]. As shown in Table 2, the v_P of Bi_2S_3 and all thermoelectric materials with low lattice thermal conductivities are larger than 0.25, indicating that there is strong ionic bonding between the atoms in the materials (the weak bonding interaction). The Grüneisen constant (γ) has a strong link with the lattice vibration anharmonicity. As far as we know, the ultralow thermal conductivity of SnSe, with a large γ of $\sim$ 3.13, stems from the lattice vibration anharmonicity in the crystal owing to the lone pair electrons of Sn. The Grüneisen constant for Bi_2S_3 is larger than that for BiCuSeO (1.5) and is comparable to that for Bi_2Se_3 (1.65) and $K_2Bi_8Se_{13}$ (1.77). The Debye temperature (θ_D) is also one of the most significant parameters to reflect the low thermal conductivity, other than the elastic properties (phonon velocity, Young's modulus, shear modulus and Grüneisen constant) that we discussed above. The Debye temperature of Bi_2S_3 is 182 K, which is lower than that of BiCuSeO (243 K) and Bi_2Se_3 (205 K), as listed in Table 2. Herein, the weak bonding interaction and the lattice vibration anharmonicity in the material's crystal lead to the intrinsically low thermal conductivity of Bi_2S_3.

The dimensionless figure of merit (ZT) as a function of measured temperature for Bi_2S_3 + x mol% $InCl_3$ (x = 0, 0.25, 0.5, 1.0 and 1.5) is shown in Fig. 4d. The ZT values for all Bi_2S_3 samples increase with the temperature, and by combing the significantly enhanced power factor and the intrinsically low thermal conductivity, finally, a maximum ZT value of 0.57 is obtained at 673 K, which is almost four times higher than that of pristine Bi_2S_3 (0.14 at 673 K). This is also a relatively high value in Bi_2S_3 system. The thermoelectric properties of Bi_2S_3 could be further enhanced by composting with high electrical conductivity materials and co-doping. This work showed the Bi_2S_3-based materials have the possibility to be a candidate of high-performance thermoelectric.

Conclusion

Bi_2S_3-based materials with high performance were prepared via $InCl_3$ doping by ball milling and spark plasma sintering. $InCl_3$ is an n-type dopant that can efficiently increase the electrical conductivity of Bi_2S_3, especially for the Bi_2S_3 + 1.0 mol% $InCl_3$ bulk sample, with a value up to 62 Scm^{-1} at 673 K. Finally, a maximum ZT value of 0.57 is obtained at 673 K along the parallel to the press direction for the sample doped with 1.0 mol% $InCl_3$ because of the remarkably enhanced power factor (363 μW m^{-1} K^{-2} at 673 K) and the intrinsically low thermal conductivity (0.43 W m^{-1} K^{-1} at 673 K). The improved thermoelectric performance of Bi_2S_3 is ascribed to the enhanced electrical transport properties via the introduction of $InCl_3$ elements.

Compliance with ethical standards

Conflict of interest There are no conflicts to declare.

References

[1] Hayder A-M, Gao M (2017) Effective use of thermal energy at both hot and cold side of thermoelectric module for developing efficient thermoelectric water distillation system. Energy Convers Manag 133:14–19

[2] Bell LE (2008) Cooling, heating, generating power, and recovering waste heat with thermoelectric systems. Science 321:1457–1461

[3] Zhou C, Dun C, Wang K, Zhang X, Shi Z, Liu G, Hewitt CA, Qiao G, Carroll DL (2016) General method of synthesis ultrathin ternary metal chalcogenide nanowires for potential thermoelectric applications. Nano Energy 30:709–716

[4] Kang H, Li J, Liu Y, Guo E, Chen Z, Liu D, Fan G, Zhang Y, Jiang X, Wang T (2018) Optimizing the thermoelectric transport properties of BiCuSeO via doping with the rare-earth variable-valence element Yb. J Mater Chem C 6:8479–8487

[5] Pei YL, Wu H, Wu D, Zheng F, He J (2014) High thermoelectric performance realized in a BiCuSeO system by improving carrier mobility through 3D modulation doping. J Am Chem Soc 136:13902–13908

[6] Ge Z-H, Qin P, He D, Chong X, Feng D, Ji Y-H, Feng J, He J (2017) Highly enhanced thermoelectric properties of Bi/Bi$_2$S$_3$ nanocomposites. ACS Appl Mater Interfaces 9:4828–4834

[7] Yang L, Chen ZG, Hong M, Han G, Zou J (2015) Enhanced thermoelectric performance of nanostructured Bi$_2$Te$_3$ through significant phonon scattering. ACS Appl Mater Interfaces 7:23694–23699

[8] Zhu Y, Carrete J, Meng Q-L, Huang Z, Mingo N, Jiang P, Bao X (2018) Independently tuning the power factor and thermal conductivity of SnSe via Ag$_2$S addition and nanostructuring. J Mater Chem A 6:7959–7966

[9] Pei Y, Wang H, Snyder GJ (2012) Band engineering of thermoelectric materials. Adv Mater 24:6125–6135

[10] Zhu H, Sun W, Armiento R, Lazić P, Ceder G (2014) Band structure engineering through orbital interaction for enhanced thermoelectric power factor. Appl Phys Lett 104:082107

[11] Zhao L-D, Zhang B-P, Li J-F, Zhou M, Liu W-S, Liu J (2008) Thermoelectric and mechanical properties of nano-SiC-dispersed Bi$_2$Te$_3$ fabricated by mechanical alloying and spark plasma sintering. J Alloys Compd 455:259–264

[12] Wu HJ, Zhao LD, Zheng FS, Wu D, Pei YL, Tong X, Kanatzidis MG, He JQ (2014) Broad temperature plateau for thermoelectric figure of merit ZT > 2 in phase-separated PbTe0.7S0.3. Nat Commun 5:4515

[13] Biswas K, Zhao L-D, Kanatzidis MG (2012) Tellurium-free thermoelectric: the anisotropic n-type semiconductor Bi$_2$S$_3$. Adv Energy Mater 2:634–638

[14] Chang C, Xiao Y, Zhang X, Pei Y, Li F, Ma S, Yuan B, Liu Y, Gong S, Zhao L-D (2016) High performance thermoelectrics from earth-abundant materials: enhanced figure of merit in PbS through nanostructuring grain size. J Alloys Compd 664:411–416

[15] Cheng X, Wang L, Wang X, Chen G (2018) Flexible films of poly(3,4-ethylenedioxythiophene):poly(styrenesulfonate)/SnS nanobelt thermoelectric composites. Compos Sci Technol 155:247–251

[16] Xie H, Su X, Zheng G, Zhu T, Yin K, Yan Y, Uher C, Kanatzidis MG, Tang X (2017) The role of Zn in chalcopyrite CuFeS$_2$: enhanced thermoelectric properties of Cu$_{1-x}$Zn$_x$FeS$_2$ with in situ nanoprecipitates. Adv Energy Mater 7:1601299

[17] Zhang R-z, Chen K, Du B, Reece MJ (2017) Screening for Cu–S based thermoelectric materials using crystal structure features. J Mater Chem A 5:5013–5019

[18] Ge ZH, Song D, Chong X, Zheng F, Jin L, Qian X, Zheng L, Dunin-Borkowski RE, Qin P, Feng J, Zhao LD (2017) Boosting the thermoelectric performance of (Na, K)-codoped polycrystalline SnSe by synergistic tailoring of the band structure and atomic-scale defect phonon scattering. J Am Chem Soc 139:9714–9720

[19] Li F, Wang W, Ge ZH, Zheng Z, Luo J, Fan P, Li B (2018) Enhanced thermoelectric properties of polycrystalline SnSe via LaCl(3) doping. Materials 11:203

[20] Zhao LD, Lo SH, Zhang Y, Sun H, Tan G, Uher C, Wolverton C, Dravid VP, Kanatzidis MG (2014) Ultralow thermal conductivity and high thermoelectric figure of merit in SnSe crystals. Nature 508:373

[21] Li J, Sui J, Pei Y, Meng X, Berardan D, Dragoe N, Cai W, Zhao L-D (2014) The roles of Na doping in BiCuSeO oxyselenides as a thermoelectric material. J Mater Chem A 2:4903–4906

[22] Zhao L-D, He J, Berardan D, Lin Y, Li J-F, Nan C-W, Dragoe N (2014) BiCuSeO oxyselenides: new promising thermoelectric materials. Energy Environ Sci 7:2900–2924

[23] Liu R, Lan J-l, Tan X, Liu Y-c, Ren G-k, Liu C, Zhou Z-f, Nan C-w, Lin Y-h (2018) Carrier concentration optimization for thermoelectric performance enhancement in n-type Bi$_2$O$_2$Se. J Eur Ceram Soc 38:2472–2746

[24] Tan X, Liu Y, Hu K, Ren G, Li Y, Liu R, Lin Y-H, Lan J-L, Nan C-W (2017) Synergistically optimizing electrical and thermal transport properties of Bi$_2$O$_2$Se ceramics by Te-substitution. J Am Ceram Soc 101:326–333

[25] Liu Z, Pei Y, Geng H, Zhou J, Meng X, Cai W, Liu W, Sui J (2015) Enhanced thermoelectric performance of Bi$_2$S$_3$ by synergistical action of bromine substitution and copper nanoparticles. Nano Energy 13:554–562

[26] Yang J, Liu G, Yan J, Zhang X, Shi Z, Qiao G (2017) Enhanced the thermoelectric properties of n -type Bi$_2$S$_3$ polycrystalline by iodine doping. J Alloys Compd 728:351

[27] Meng Q-L, Kong S, Huang Z, Zhu Y, Liu H-C, Lu X, Jiang P, Bao X (2016) Simultaneous enhancement in the power

factor and thermoelectric performance of copper sulfide by In$_2$S$_3$ doping. J Mater Chem A 4:12624–12629

[28] Tsutsui M, Zhang LT, Ito K, Yamaguchi M (2004) Effects of in-doping on the thermoelectric properties of β-Zn$_4$Sb$_3$. Intermetallics 12:809–813

[29] Zhang Q, Liao B, Lan Y, Lukas K, Liu W, Esfarjani K, Opeil C, Broido D, Chen G, Ren Z (2013) High thermoelectric performance by resonant dopant indium in nanostructured SnTe. Proc Natl Acad Sci USA 110:13261–13266

[30] Ge ZH, Zhang BP, Liu Y, Li JF (2012) Nanostructured Bi(2−x)Cu(x)S3 bulk materials with enhanced thermoelectric performance. Phys Chem Chem Phys 14:4475–4481

[31] Guo J, Ge Z, Hu M, Qin P, Feng J (2018) Facile synthesis of NaBiS$_2$ nanoribbons as a promising visible light-driven photocatalyst. Phys Status Solidi-R 12:1800135

[32] López R, Gómez R (2011) Band-gap energy estimation from diffuse reflectance measurements on sol–gel and commercial TiO$_2$: a comparative study. J Sol–Gel Sci Technol 61:1–7

[33] Pei J, Zhang L-J, Zhang B-P, Shang P-P, Liu Y-C (2017) Enhancing the thermoelectric performance of CexBi$_2$S$_3$ by optimizing the carrier concentration combined with band engineering. J Mater Chem C 5:12492–12499

[34] Du X, Cai F, Wang X (2014) Enhanced thermoelectric performance of chloride doped bismuth sulfide prepared by mechanical alloying and spark plasma sintering. J Alloys Compd 587:6–9

[35] Morin FJ, Maita JP (1954) Conductivity and Hall effect in the intrinsic range of germanium. Phys Rev 94:1525

[36] Morin FJ, Maita JP (1954) Electrical properties of silicon containing arsenic and boron. Phys Rev 96:28

[37] Heremans JP, Jovovic V, Toberer ES, Saramat A, Kurosaki K, Charoenphakdee A, Yamanaka S, Snyder GJ (2008) Enhancement of thermoelectric efficiency in PbTe by distortion of the electronic density of states. Science 321:554–557

[38] Wan CL, Pan W, Xu Q, Qin YX, Wang JD, Qu ZX, Fang MH (2006) Effect of point defects on the thermal transport properties of (La$_x$Gd$_{1−x}$)2Zr$_2$O$_7$: experiment and theoretical model. Phys Rev B 74:144109

[39] Kurosaki K, Kosuga A, Muta H, Uno M, Yamanaka S (2005) Ag$_9$T$_1$Te$_5$: a high-performance thermoelectric bulk material with extremely low thermal conductivity. Appl Phys Lett 87:061919

[40] Liu X, Wang D, Wu H, Wang J, Zhang Y, Wang G, Pennycook SJ, Zhao L-D (2018) Intrinsically low thermal conductivity in BiSbSe$_3$: a promising thermoelectric material with multiple conduction bands. Adv Funct Mater 29:1806558

[41] Xiao Y, Chang C, Pei Y, Wu D, Peng K, Zhou X, Gong S, He J (2016) Origin of low thermal conductivity in SnSe. Phys Rev B 94:125203

[42] Anderson OL (1963) A simplified method for calculating the Debye temperature from elastic constants. J Phys Chem Solids 24:909–917

[43] Ge C, Hu M, Wu P, Tan Q, Chen Z, Wang Y, Shi J, Feng J (2018) Ultralow thermal conductivity and ultrahigh thermal expansion of single-crystal organic-inorganic hybrid perovskite CH$_3$NH$_3$PbX$_3$ (X = Cl, Br, I). J Phys Chem C 122:15973–15978

[44] Koc H, Ozisik H, Deligoz E, Mamedov AM, Ozbay E (2014) Mechanical, electronic, and optical properties of Bi(2)S(3) and Bi(2)Se(3) compounds: first principle investigations. J Mol Model 20:2180

[45] Gao X, Zhou M, Cheng Y, Ji G (2016) First-principles study of structural, elastic, electronic and thermodynamic properties of topological insulator Bi$_2$Se$_3$ under pressure. Philos Mag 96:208–222

[46] Pei Y, Chang C, Wang Z, Yin M, Wu M, Tan G, Wu H, Chen Y, Zheng L, Gong S, Zhu T, Zhao X, Huang L, He J, Kanatzidis MG, Zhao LD (2016) Multiple converged conduction bands in K$_2$Bi$_8$Se$_{13}$: a promising thermoelectric material with extremely low thermal conductivity. J Am Chem Soc 138:16364–16371